RSC Advances

PAPER

View Article Online
View Journal | View Issue

Cite this: *RSC Adv.*, 2018, **8**, 19852

Hierarchically porous SiO_2/C hollow microspheres: a highly efficient adsorbent for Congo Red removal†

Jie Wang,[a] Longya Xiao,[a] Shuai Wen,[a] Nuo Chen,[a] Zhiyin Dai,[a] Junyang Deng,[a] Longhui Nie *[ab] and Jie Min*[a]

Received 7th April 2018
Accepted 17th May 2018

DOI: 10.1039/c8ra02988a

rsc.li/rsc-advances

Hierarchically porous SiO_2/C hollow microspheres (HPSCHMs) were synthesized by a hydrothermal and NaOH-etching combined route. The adsorption performance of the prepared HPSCHMs was investigated to remove Congo Red (CR) in aqueous solution. The results show that the synthesized composite possesses a hollow microspherical structure with hierarchical pores and a diameter of about 100–200 nm, and its surface area is up to 1154 $m^2\ g^{-1}$. This material exhibits a remarkable adsorption performance for CR in solution, and its maximum adsorption amount for CR can reach up to 2512 mg g^{-1}. It shows faster adsorption and much higher adsorption capacity than the commercial AC and γ-Al_2O_3 samples under the same conditions. The studies of the kinetics and thermodynamics indicate that the adsorption of CR on the PHSCHM sample obeys the pseudo-second order model well and belongs to physisorption. The adsorption activation energy is about 7.72 kJ mol^{-1}. In view of the hierarchically meso–macroporous structure, large surface area and pore volume, the HPSCHM material could be a promising adsorbent for removal of pollutants, and it could also be used as a catalyst support.

1. Introduction

Hierarchically porous carbon hollow microspheres (HPCHMs) have attracted a great deal of attention due to their advantages including large specific surface area, low density and special porous structure.[1–4] HPCHMs as a promising material can be widely used in many fields such as adsorption,[1] catalysis,[3] fuel cells[4] and nano devices.[5] Many strategies have been developed to design and prepare HPCHMs.[1–7] Among them, hard-template and soft-template methods have been widely adopted to fabricate HPCHMs. For instance, uniform HPCHMs were synthesized using a hard template and confined nanospace pyrolysis method.[1] Recently, monodispersed mesoporous carbon hollow spheres were successfully prepared by a facile one-step method.[6] The synthesized hollow carbon spheres possessed a high specific surface area of 2106–2225 $m^2\ g^{-1}$ and large pore volume of 1.95–2.53 $cm^3\ g^{-1}$ with an open interconnected mesoporous shell, which are beneficial for effective diffusion and adsorption of molecules as well as loading active guest species. These structure features indicate that this material would be a promising candidate in the fields of adsorption and catalysis. However, in the last step of this preparation for carbon hollow spheres, silica needed to be removed in 15% HF aqueous solution, which is extremely harmful to the surroundings.

In order to overcome the drawback of using HF solution for silica removal, in this work, the hierarchically porous SiO_2/C hollow microspheres were prepared by a modified preparation method in combination with NaOH-etching strategy to remove part of the silica. The resulted SiO_2/carbon hollow microspheres possessed a high surface area and hierarchically meso–macroporous structure. The remaining SiO_2 in the composite also can be served as the adsorption site.[8,9] Therefore, in this work, we tried to extend the application of SiO_2/carbon hollow microspheres in the field of adsorption. The adsorption performance of the prepared sample was evaluated by adsorption of CR in aqueous solution (a typical and harmful organic pollutant in water). The prepared HPSCHMs sample exhibited excellent adsorption performance for CR in water. The studies of kinetics and thermodynamics of the CR adsorption over the HPSCHMs sample were also performed.

2. Experimental

2.1 Preparation of hollow SiO_2/carbon composite microspheres

The hollow SiO_2/carbon composite microspheres were prepared by a modified method.[6] In a typical synthesis, resorcinol (0.4 g) and CTAB (1.2 g) were added into a mixing solution of deionized

[a]Hubei Provincial Key Laboratory of Green Materials for Light Industry, Hubei University of Technology, Wuhan 430068, P. R. China. E-mail: nielonghui@mail.hbut.edu.cn; whutminj@163.com; Tel: +86 59750482

[b]Collaborative Innovation Center of Green Light-weight Materials and Processing, Hubei University of Technology, Wuhan 430068, P. R. China

† Electronic supplementary information (ESI) available. See DOI: 10.1039/c8ra02988a

water (44 mL) and ethanol (16 mL) at room temperature under vigorous stirring. After compete dissolution of reagents, 0.4 mL of NH_4OH (25–28 wt%) solution was dropped into above solution, and the mixture was kept continuously stirring for 20 min, followed by the addition of the formaldehyde solution (0.56 mL). Then, the solution was kept standing still for 10 min to form an emulsion. Subsequently, 2 mL of TEOS was dropped into the above solution and stirred for 24 h at room temperature. The resulting solution was heated for 24 h at 80 °C under a static condition in a Teflon-lined autoclave. The product was collected by centrifugation, washed by deionized water and ethanol for several times, dried in air and annealed at 850 °C for 3 h with the ramp rate of 1 °C min^{-1} in nitrogen atmosphere. The obtained sample was further treated for 24 h at 80 °C in 3 M of NaOH solution to remove part of silica. Finally, the hierarchically porous SiO_2/carbon hollow microspheres (denoted as HPSCHMs) were obtained.

2.2 Characterization

The crystal structure of as-prepared samples was analyzed on a D8X X-ray diffractometer (Bruker) with Cu K_α radiation at a scan rate (2θ) of 0.05° s^{-1}. A Raman spectrum was acquired by THMS60 with excitation wavelength of 532 nm. The morphology and microstructure of the prepared samples were observed on a JSM-7500F field emission scanning electron microscope (FE-SEM, JEOL, Japan) at an accelerating voltage of 15 kV and a JEM-2100F microscope at an accelerating voltage of 200 kV. The chemical composition and element valence was analyzed by X-ray photoelectron spectroscopy (XPS) spectra performed on a VG ESCALAB250xi with X-ray monochromatisation. The C 1s peak at 284.8 eV of the surface adventitious carbon was used as a reference for all binding energies (BE). Nitrogen adsorption data were acquired by a Micromeritics ASAP 2020 nitrogen adsorption apparatus (USA). All the samples were pretreated at 180 °C for 3 h before nitrogen adsorption measurements. The Brunauer–Emmett–Teller (BET) surface area (S_{BET}) of the samples was evaluated by a multipoint method using adsorption data in the relative pressure (P/P_0) range of 0.05–0.3. The pore size distribution (d_{pore}) was obtained from adsorption data by the Barrett–Joyner–Halenda (BJH) method. The single-point pore volume (V_{pore}) was acquired from nitrogen adsorption volume at the relative pressure of 0.98. The Fourier transformations infrared spectroscopy (FTIR) measurement was performed out on a Thermo Fisher iS50 instrument. Scans were collected from 4000 to 400 cm^{-1} with a resolution of 4 cm^{-1}.

2.3 Adsorption experiments for Congo Red

Adsorption experiments for Congo Red ($C_{32}H_{22}N_6O_6S_2Na_2$) over the samples were performed as follows: 10 mg of the samples were added into 100 mL of CR solution (20–100 mg L^{-1}) under stirring at pH = 7.0 and 30 °C. At different adsorption time, the suspension was separated by centrifugation, and analytical samples were taken from the top clear liquid. The CR concentration was determined by a spectrophotometric method. The amount of CR adsorbed per unit mass of the adsorbent was calculated by the following equation:

$$q_t = \frac{(c_0 - c_t)V}{m}$$

where q_t (mg g^{-1}) is the amount adsorbed per gram of adsorbent at adsorption time t (min), c_0 is the initial CR concentration (mg L^{-1}), c_t is the CR concentration at adsorption time t (mg L^{-1}), V is the volume of solution (L), and m is the mass of adsorbent (g).

3. Results and discussion

3.1 Crystal phase, morphology and textural properties

The XRD pattern of the HPSCHMs sample (Fig. 1a) reveals two weak characteristic peaks at 2θ of 24.2° and 42.7°, which can be attributed to the (002) and (101) planes of graphite carbon (JCPDF card 75-1621), respectively. The Raman spectrum of the HPSCHMs sample (Fig. 1b) shows two bands at 1593 cm^{-1} (G-band, resulted from graphitic carbon) and 1336 cm^{-1} (D-band, attributed to defects), further confirming the presence of graphitic carbon in the composite. The intensity of the G-band is higher than that of the D-band, indicating relatively higher graphitized content in the sample.[10,11]

The morphology and micro-structure of the HPSCHMs sample were analyzed by FESEM and TEM (shown in Fig. 2).

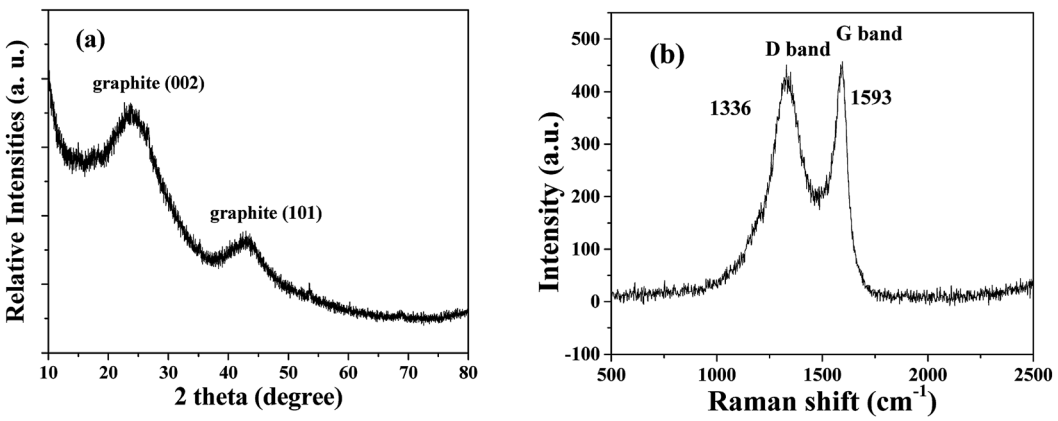

Fig. 1 XRD pattern (a) and Raman pattern (b) of HPSCHMs.

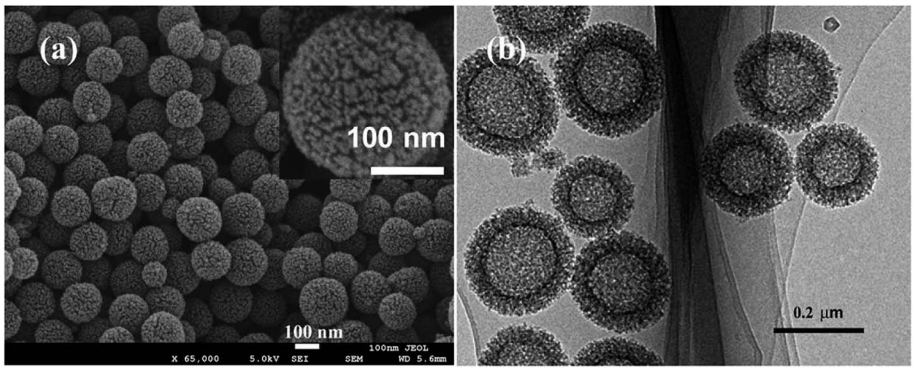

Fig. 2 SEM (a) and TEM (b) images of HPSCHMs.

FESEM images (Fig. 2a and its inset) of HPSCHMs show that they are composed of many porous microspheres with the diameter of about 80–200 nm. The TEM image (Fig. 2b) exhibits that the microspheres are hollow with shell wall of about 40 nm thick and void core of about 80–120 nm in diameter. The EDX result (Fig. 3) exhibits that C, O, and Si elements coexist in the HPSCHMs sample, indicating part of SiO_2 was remained in the composite after NaOH-etching treatment. How were the porous microspheres formed? In the preparation of hollow SiO_2/carbon composite microspheres, resorcinol and formaldehyde reacted rapidly under the action of ammonia molecule catalyst in a water/alcohol solution to generate numerous hydroxymethyl-substituted species, which further acted with surfactant CTAB to form droplets of emulsion. When TEOS as SiO_2 precursor was added, a strong electrostatic interface action took place between silicate anions and surfactant CTAB molecule cations. Finally, a "interpenetration twin" spherical structure was formed through the hydrolysis, cross-linking and condensation of TEOS and resorcinol–formaldehyde (RF) precursors.[6] During this process, TEOS can avoid excessive cross-linking between RF micelles by the diffusion of silicates into the emulsion droplets, so that hollow nanospheres were obtained. On the other hand, the inorganic silica can greatly reduce the structural shrinkage of the carbon precursor during high-temperature calcination. Porous structure was formed by the release of gas during high-temperature calcination and the removal of SiO_2 with the etching of NaOH.

The chemical composition and chemical status of the HPSCHMs sample were analyzed by the XPS analysis. The survey spectrum (not shown here) shows that the HPSCHMs sample is mainly consisted of C, O, Na and Si elements, which is

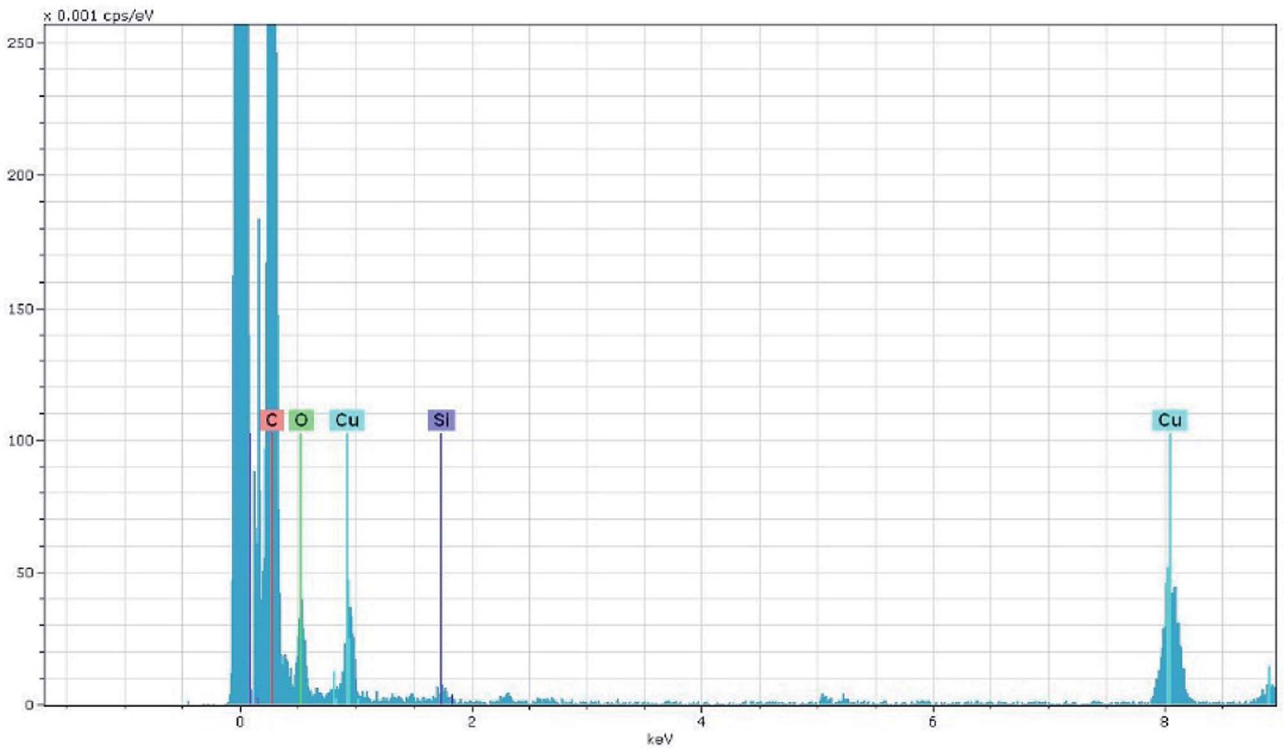

Fig. 3 EDX pattern of HPSCHMs.

almost consistent with the results of EDX analysis. Na element comes from the residual of NaOH. The contents of C, O, Na and Si elements are shown in Table S1,† which suggests that the HPSCHMs sample was mainly composed of C and O elements. Most of SiO_2 was removed during the process of NaOH etching. Also, the high O content (11.26%) indicates the presence of abundant oxygen-containing groups on the surface of the HPSCHMs sample. The high-resolution XPS spectra of C, O, and Si elements are shown in Fig. 4. In the C 1s spectra (see Fig. 4a), there are three fitted peaks at 284.77, 285.58 and 288.94 eV, respectively. The main peak at 284.77 eV is attributed to the C–C or C–H species, and the smaller peaks at 285.58 and 288.94 eV are ascribed to the C–O and –O–C=O bonds, respectively.[12] Fig. 4b reveals that the O 1s high resolution XPS spectrum can be deconvolved into three peaks at binding energies of 530.78, 532.18, and 533.61 eV. The peak at 530.78 eV is assigned to O 1s of hydroxyl groups. The peak appeared at 532.18 eV comes from O 1s of C=O groups,[12] physisorbed water[13] and SiO_2.[14] And the peak at 533.61 eV is attributed to the C–O groups.[12] In Fig. 4c, the peak at 102.4 eV is assigned to Si 2p for SiO_2.[15] The XPS results confirmed that the SiO_2 was remained in the HPSCHMs sample after NaOH treatment.

FTIR spectra of hollow SiO_2/carbon composite microspheres before and after NaOH etching are shown in Fig. S1.† For the hollow SiO_2/carbon composite microspheres before NaOH etching, a weak band at around 3430 cm^{-1} and a peak at around 1580 cm^{-1} can be observed, which belong to O–H groups (such as C–OH, Si–OH).[16] The weak peaks at 2931 and 2847 cm^{-1} are attributed to C–H bonds, which shows that most of hydrogen species in the precursor were removed during high-temperature calcination. The strong peaks at around 1113 and 467 cm^{-1} confirms the existence of SiO_2.[16–18] While the peak at 840 cm^{-1} is assigned to Si–C bond,[16] which indicates the interaction between carbon precursors and SiO_2 existed during high-temperature calcination. However, in the FTIR spectrum of the hollow SiO_2/carbon composite microspheres after NaOH etching, the peak intensities for Si–O–Si decreased obviously, and the peak intensities for O–H groups increased greatly, indicating that most of SiO_2 was removed and the Si–OH bond formed during the interaction of NaOH and SiO_2. Also, no obvious change in the peak of Si–C bond before and after NaOH etching indicates that SiO_2 bonded to C was remained in the HPSCHMs sample during the interaction of NaOH and SiO_2. Combination of the results of XRD, XPS and FTIR analysis, most of C elements in the HPSCHMs sample exist as the form of graphite carbon, a small part of C elements may exist as organic compounds with C–H, C–O or –O–C=O bonds. The existence of C–Si bond shows that the C–Si species may be a part of the PHSCHMs sample. It is worth to mention that the existence of abundant oxygen-containing groups (–OH, –CO and –O–C=O) benefits the improvement of adsorption performance.[19] The FTIR spectrum of the HPSCHMs sample after adsorption of CR is also shown in Fig. S1.† A new peak at 1050 cm^{-1} can be assigned to the symmetric stretching vibration peak of sulfonate group (SO_3^-) of CR, suggesting that the interactions between the adsorbed CR and the HPSCHMs sample are through the sulfonate groups.[20]

Fig. 5 shows nitrogen adsorption–desorption isotherm and pore size distribution curve for the HPSCHMs sample. The nitrogen adsorption–desorption isotherm belongs to type IV according to the IUPAC classification,[21] suggesting the existence of mesopores. The type H3 of hysteresis loops for HPSCHMs can be observed at P/P_0 range of 0.4–1.0, which implies the presence of slit-like pores. The high adsorption values at relative pressure approaching 1.0 indicates the presence of mesopores and macropores.[22,23] The pore-size distribution curve calculated from the adsorption branch shows that the HPSCHMs sample has a smaller pore distribution with peak pore at *ca.* 3 nm and a larger pore distribution (50–100 nm). The macroporous structure of HPSCHMs can be observed directly by FESEM and TEM. The HPSCHMs sample shows a lot of open slit-like pores with a cavity with diameter of 80–120 nm (Fig. 2). These open macroporous channels can act as ideal transport routes for liquid and gas molecules into the interior surface of the sample. The BET surface area (S_{BET}), pore volume (V_{pore}) and pore size (d_{pore}) of HPSCHMs (Table 1) are 1127 $m^2\ g^{-1}$, 1.29 $cm^3\ g^{-1}$ and 4.6 nm, respectively. From Table 1, it also shows that the HPSCHMs sample has much bigger surface area and pore volume compared with commercial AC and γ-Al_2O_3, which are of importance to the adsorption of pollutants in aqueous solution.

3.2 A comparison of adsorption capacity

A contrast of adsorption performance of the HPSCHMs, AC and γ-Al_2O_3 samples for aqueous CR solution is shown in Fig. 6.

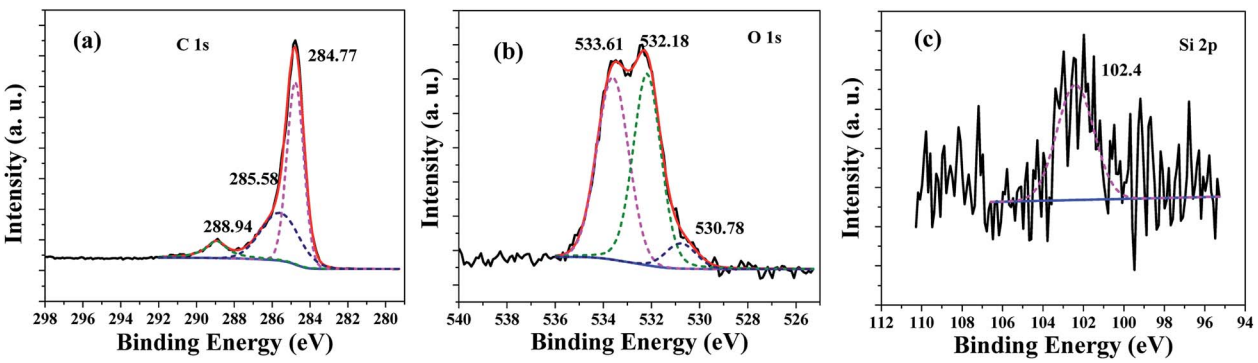

Fig. 4 High-resolution XPS spectra for C 1s (a), O 1s (b) and Si 2p (c) of the HPSCHMs sample.

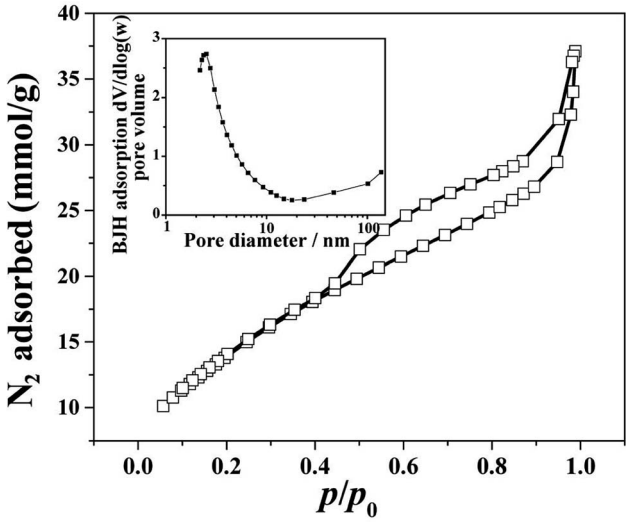

Fig. 5 Nitrogen adsorption–desorption isotherm and the corresponding pore-size distribution curve (inset) of HPSCHMs.

Table 1 Basic parameters for the as-synthesized and commercial samples

Sample	S_{BET} ($m^2\ g^{-1}$)	V_{pore} ($cm^3\ g^{-1}$)	d_{pore} (nm)
HPSCHMs	1127	1.29	4.6
AC	492	0.41	3.3
γ-Al_2O_3	203	0.47	9.3

After 2160 min adsorption, the adsorption equilibrium nearly reached over the HPSCHMs sample, but it did not over the AC and γ-Al_2O_3 samples (see Fig. 5). The results indicate faster adsorption of CR over the former. The adsorption amounts of the HPSCHMs, AC and γ-Al_2O_3 samples for CR at 2160 min are 788.7, 183.7, and 287 mg g^{-1}, respectively, which show much higher adsorption capacity of the HPSCHMs sample compared with the other two samples.

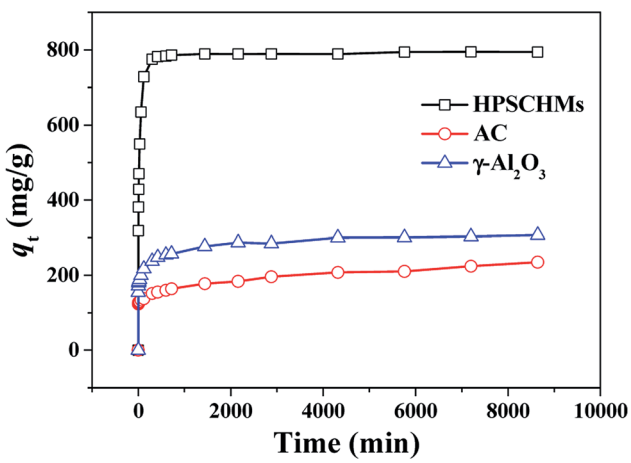

Fig. 6 Comparison of adsorption capacities on HPSCHMs, AC and γ-Al_2O_3 for CR.

3.3 Adsorption kinetics

The study of adsorption kinetics can provide valuable data to understand the sorption mechanism.[24] The adsorption tests at different CR concentration were performed over the PHSCHMs sample. The adsorption isotherms at different CR concentrations at 30 °C are shown in Fig. 7. It can be observed that adsorption in all the experiments was fast in the initial 120 min. Then, the adsorption rates gradually decreased and adsorption was in equilibrium at about 1000 min.

In the study of the kinetics of the adsorption process, kinetics of CR onto the PHSCHMs sample was investigated by the pseudo-first-order and pseudo-second-order kinetic models, and the intraparticle diffusion model was further examined to analyze the diffusion mechanism of the adsorption process.

The pseudo-first-order kinetic model has been widely applied to analyze sorption kinetics. Pseudo-first-order kinetic equation can be expressed as:

$$\ln(q_e - q_t) = \ln q_e - k_1 t$$

where k_1 (min^{-1}) is the rate constant of pseudo-first-order reaction, q_e and q_t (mg g^{-1}) are the adsorption amount of CR onto the PHSCHMs sample at equilibrium and time t (min), respectively. The plot of $\ln(q_e - q_t)$ against t is shown in Fig. 8a. From the slope, k_1 can be obtained. The values of k_1 and correlation coefficient (R^2) are listed in Table S2.† The values of R^2 changed from 0.8001 to 0.9503, which indicate that the adsorption of CR on the PHSCHMs sample fits the pseudo-first-order reaction not well.

Pseudo-second-order kinetic equation can be expressed as:

$$\frac{t}{q_t} = \frac{1}{k_2 q_e^2} + \left(\frac{1}{q_e}\right) t$$

where k_2 (g (mg min)$^{-1}$) is the rate constant of pseudo-first-order reaction.

The plot of t/q_t against t is shown in Fig. 8b. q_e and k_2 can be calculated from the slope and intercept. The values of R^2 (see Table S2†) are close to 1, which suggests that the adsorption kinetics obeys pseudo-second order model very well.

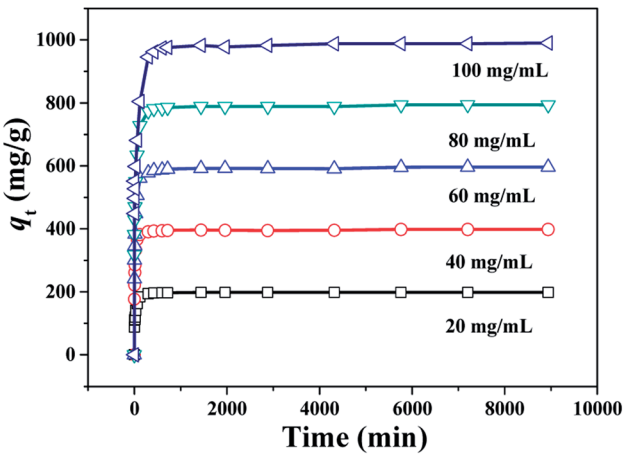

Fig. 7 Changes of adsorption capacity with adsorption time for CR over the HPSCHMs sample at different initial CR concentrations (adsorbent dose: 100 mg L^{-1}; 30 °C; pH = 7).

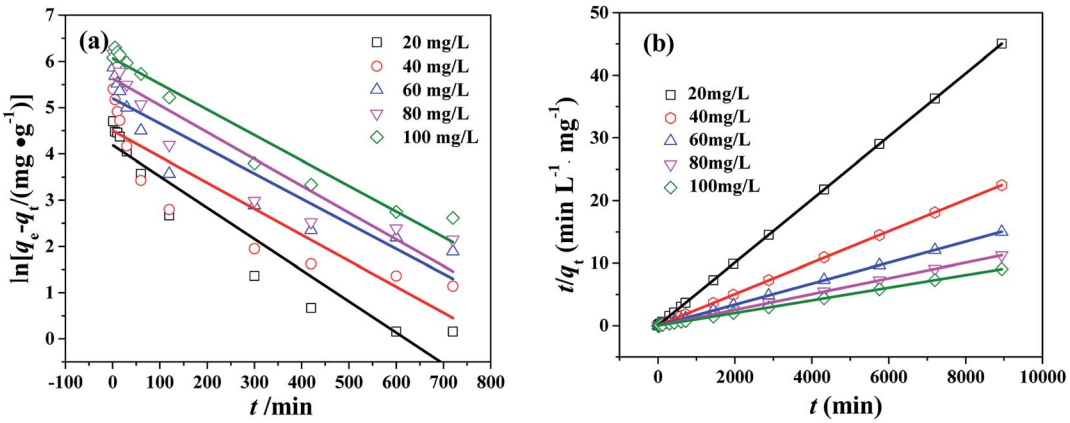

Fig. 8 Pseudo-first-order kinetics (a) and pseudo-second-order kinetics (b) for CR adsorption over the HPSCHMs sample at different initial CR concentrations (T = 30 °C; adsorbent dose: 100 mg L^{-1}; pH = 7).

To determine the diffusion mechanism, intra-particle diffusion kinetic model was applied to examine CR adsorption on PHSCHMs. The model equation is expressed as:

$$q_t = k_{di}t^{0.5} + C_i$$

where k_{di} (mg g^{-1} min$^{-0.5}$) is the rate constant of stage i, which is acquired from the slope of the plot of q_t against $t^{0.5}$ (Fig. 9). C_i is the intercept of stage i, which is a parameter about the thickness of boundary layer. The linear fits of q_t against $t^{0.5}$ indicate that intraparticle diffusion model works for the adsorption of CR on PHSCHMs at different initial concentrations, and the intraparticle diffusion is the rate limiting process. The three-linear plots show that adsorption process includes three steps. The first sharp step is related with the instantaneous adsorption stage (k_{d1}), in which adsorption mainly takes place on the external surface of the PHSCHMs sample. The adsorption is fast, which is due to the big concentration gradient in this stage to produce large driving force for CR diffusion to the external surface of the PHSCHMs sample from the solution. The second stage (k_{d2}) is the intra-particle diffusion region which is the rate limiting step due to the slow adsorption. The third stage (k_{d3}) is the final equilibrium region in which intra-particle diffusion rate further decreases due to the very low concentration of CR remained in the solutions. Therefore, CR is slowly transported onto the inner surface of the small nanopores. Table S3† lists the intraparticle diffusion rate parameters in different stages for CR adsorption with different initial concentrations over the PHSCHMs sample at 30 °C. The decreasing values of k_d ($k_{d1} > k_{d2} > k_{d3}$) is due to the gradually decreasing CR concentration with adsorption time.

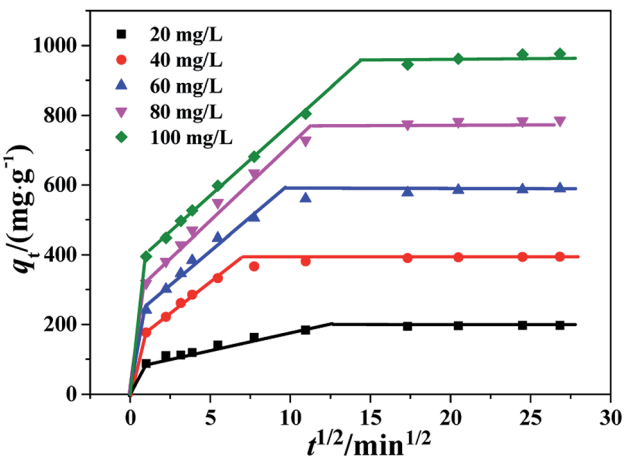

Fig. 9 Intra-particle diffusion kinetics of the PHSCHMs sample for CR adsorption at different initial concentrations.

3.4 Adsorption isotherms

Adsorption isotherms were used to study the adsorption capacity of the sample at different equilibrium CR concentrations. Here, Langmuir and Freundlich isotherms were performed to fit the equilibrium data. In the assumption of Langmuir model, all the adsorption sites are uniform and only monolayer adsorption takes place. The Langmuir isotherm equation is expressed as:

$$\frac{C_e}{q_e} = \frac{1}{q_{max}K_L} + \frac{1}{q_{max}}C_e$$

where q_e (mg g^{-1}) is the equilibrium adsorption amount of CR on per unit mass of adsorbent, C_e (mg L^{-1}) is the equilibrium concentration of CR, q_{max} (mg g^{-1}) is the theoretical maximum adsorption capacity, and K_L (L mg^{-1}) is the Langmuir adsorption constant. The values of q_{max} and K_L can be calculated from the slope and intercept of the linear plot of C_e/q_e against C_e.

The fundamental characteristics of Langmuir isotherm can be expressed by a dimensionless separation factor (R_L), defined as:

$$R_L = \frac{1}{1 + K_L C_0}$$

In the assumption of Freundlich adsorption model, adsorption occurs on a heterogeneous surfaces. Freundlich isotherm is not restricted to monolayer adsorption and multi-molecule adsorption can be also observed. The Freundlich adsorption isotherm equation is an empirical equation and is expressed as:

$$\log q_e = \log K_F + \left(\frac{1}{n}\right)\log C_e$$

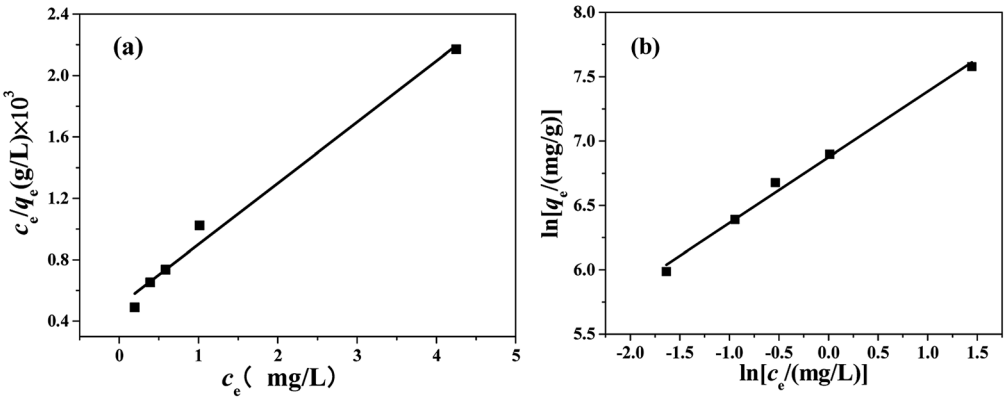

Fig. 10 Langmuir (a) and Freundlich (b) isotherms of the HPSCHMs sample for CR adsorption at 30 °C.

where k_F and $1/n$ are the Freundlich constant and the heterogeneity factor, respectively. And they can be obtained from the intercept and slope of the linear plot ln q_e against ln c_e.

The Langmuir and Freundlich adsorption isotherms are revealed in Fig. 10. Table S4† lists the values of Langmuir and Freundlich model's parameters. The values of R_L ($R_L = 0.0063$, in the range of 0–1) and $1/n$ ($0 < 1/n < 1$) suggest that the CR adsorption over the PHSCHMs sample satisfies both Langmuir and Freundlich models.[24] The value of R^2 from the Freundlich model ($R^2 = 0.9905$) is slightly bigger than that from the Langmuir model (0.9834), indicating that the Freundlich model is somewhat better to describes the adsorption isotherm over the PHSCHMs sample.

Table 2 Comparison of CR adsorption capacities of different adsorbents from the Langmuir isotherm equation

Adsorbent	Adsorption capacities (mg g^{-1})	References
HPSCHMs	2512	This work
γ-Al_2O_3 (MWAO)	515.4	25
SBA	344.8	26
BiOI architectures	216.8	27
Fe_3O_4@meso C nanocapsules	1657	28
MgO nanoplates	303.0	29
ZnO	334	30
NiO	223.8	31
Urchin-like FeOOH	239	32
Ni/Mg/Al layered double hydroxides	1250	21
Activated carbon	189	33
Silica	294.1	34
Iron nanoparticles	1735	35
SnS/AC	384.6	36
MONT-1	823.3	37
NiO–Al_2O_3	375	38
Carbon-containing bone hydroxyapatite (CBHA)	329	39
ZnO/NiO	518	40
MgO–GO	237	41
ZnO–Al_2O_3	397	42
$NiCo_2O_4$	366	43
NiO	534.8	44
$Mg(OH)_2$–GO	118	45

From the value of q_{max} calculated from the intercept of Langmuir equation, the maximum adsorption capacity for CR on the PHSCHMs sample can be obtained to be about 2512 mg g^{-1}, which is much higher than those reported in literatures (see Table 2). From the results of N_2 adsorption–desorption, FESEM and TEM analysis, the large surface area and pore volume as well as the hierarchically porous structure of the HPSCHMs sample can account for the fast adsorption and the excellent adsorption performance for CR. The results show the HPSCHMs sample would be an excellent adsorbent for aqueous pollutants due to its high surface area and hierarchically meso–macroporous structure.

3.5 Thermodynamic study

The thermodynamic study of CR adsorption was performed in a temperature range of 30–50 °C with 100 mg L^{-1} CR and 100 mg L^{-1} of the adsorbent, and the results is shown in Fig. 11a. The pseudo-second-order reaction rate constant is related with temperature by the Arrhenius equation. Arrhenius equation can be expressed as:

$$\ln k_2 = \ln A - \frac{E_a}{RT}$$

where E_a (kJ mol^{-1}) is the activation energy, A is a pre-exponential factor, R is the gas constant (8.314 J mol^{-1} K^{-1}) and T is the temperature of the solution.

And the type of adsorption can be determined by the value of E_a. When ln k_2 is plotted against $1/T$, a straight line is obtained. From the slope of Arrhenius equation, the activation energy of adsorption can be calculated to be about 7.72 kJ mol^{-1}, indicating that the CR adsorption on the HPSCHMs sample belongs to physisorption (generally, in the range of 0–40 kJ mol^{-1}).[14]

3.6 Adsorption mechanism

Generally, several factors are mainly related to the adsorption performance of adsorbents, such as specific surface area, interaction between groups of adsorbent and adsorbate, and electrostatic attraction between adsorbate molecules and the surface of adsorbent materials.[20,35,40] Here, the HPSCHMs sample possesses large specific surface area and hierarchically porous structure, which can provide more available active

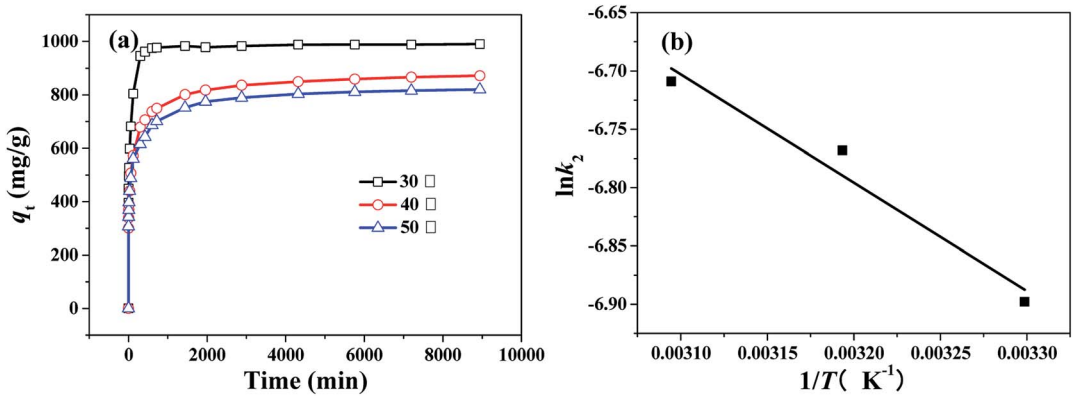

Fig. 11 (a) Changes of adsorption capacity with adsorption time for CR over the HPSCHMs sample at different temperature (adsorbent dose: 100 mg L^{-1}; pH = 7, initial CR concentration: 100 mg L^{-1}), and (b) thermodynamics fitting for CR on the HPSCHMs sample (adsorbent dose: 100 mg L^{-1}; pH = 7, initial CR concentration: 100 mg L^{-1}).

adsorption sites and efficient transport pathways, resulting in the enhancement of adsorption performance. The surface charges of the HPSCHMs sample were determined by Malvern Zetasizer Nano ZS90. Fig. S2† shows the variation in zeta potentials of the HPSCHMs sample dependence on the pH value of the suspensions. It can be seen from Fig. S2† that the isoelectric point (IEP) of the HPSCHMs sample is about 4.3 and the zeta potential value of the HPSCHMs sample is negative in neutral water environment, which indicates that electrostatic interaction seems to be an unfavorable factor for the high adsorption performance of CR on the HPSCHMs sample because the negative charge is also for the CR molecular. Based on the results of FTIR, TEM, SEM and XPS analysis, abundant oxygen-containing groups in the HPSCHMs sample can possibly interact with the groups (such as sulfonate group, SO_3^-) of CR through the weak hydrogen bonding to adsorb CR molecules.[20] From the images of SEM and TEM, the HPSCHMs sample is of porous microsphere structure with the diameter of about 80–200 nm. Although the negative surface charge of PHSCHMs firstly hinders the adsorption of CR with like charge, but it can also help the CR molecules remaining in the inside of microspheres once the CR molecules enter the inner space of the microspheres through the pores on the surface of the HPSCHMs sample due to effect of repulsive force. In sum, the HPSCHMs sample revealed the great adsorption capacity towards CR molecules mainly due to three factors: its large specific surface area, synergistic effect of porous microsphere structure and negative zeta potential, and the interaction of abundant oxygen-containing groups in the HPSCHMs sample with surface groups of CR.

4. Conclusions

Hierarchically porous SiO_2/carbon hollow microspheres were synthesized by a modified hydrothermal and NaOH-etching treatment combined route. The obtained HPSCHMs sample has the high surface area of 1127 m^2 g^{-1} and hierarchically porous structure. Therefore, an excellent adsorption performance on this material was found in the aqueous CR adsorption experiments. A faster adsorption and an much higher adsorption performance were observed over the HPSCHMs sample compared with the AC and γ-Al_2O_3 samples. The maximum adsorption amount of this material for CR is up to 2512 mg g^{-1}. The studies of the kinetics and thermodynamics indicate that the adsorption of CR on the PHSCHMs sample obeys pseudo-second order model well and belongs to physisorption. The adsorption activation energy is about 7.72 kJ mol^{-1}. The great adsorption capacity towards CR molecules on the HPSCHMs sample is mainly due to its large specific surface area, synergistic effect of porous microsphere structure and negative zeta potential, and the interaction of abundant oxygen-containing groups in the HPSCHMs sample with surface groups of CR. Considering the hierarchically meso–macroporous structure, large surface area and pore volume, the HPSCHMs material would be an excellent adsorbent for removal of pollutants, and it can be also used as the catalyst support.

Conflicts of interest

There are no conflicts to declare.

Acknowledgements

This work was supported by the Natural Science Foundation of China (51572074), Open Project of Key Laboratory of Green Light Industry Materials of Hubei Province (201710A12) and College Student Innovation Training Project of China (201610500021).

References

1 A. H. Lu, T. Sun, W. C. Li, Q. Sun, F. Han, D. H. Liu and Y. Guo, *Angew. Chem.*, 2011, **123**(49), 11969.
2 S. Li, A. Pasc, V. Fierro and A. Celzard, *J. Mater. Chem. A*, 2016, **4**, 12686.
3 S. H. Joo, S. J. Choi, I. Oh, J. Kwak, Z. Liu, O. Terasaki and R. Ryoo, *Nature*, 2001, **412**, 169.
4 J. H. Kim and J. S. Yu, *Phys. Chem. Chem. Phys.*, 2010, **12**, 15301.

5 J. Liu, N. P. Wickramaratne, S. Qiao and M. Jaroniec, *Nat. Mater.*, 2015, **14**, 763.
6 J. H. Hou, T. Cao, F. Idrees and C. B. Cao, *Nanoscale*, 2016, **8**, 451.
7 S. Zhao, X. Y. Li, C. Y. Wang and M. M. Chen, *Mater. Lett.*, 2012, **70**, 54.
8 Y. Le, D. P. Guo, B. Cheng and J. G. Yu, *Appl. Surf. Sci.*, 2013, **274**, 110.
9 H. Fu, X. Ding, C. Ren, W. Li, H. Wu and H. Yang, *RSC Adv.*, 2017, **7**, 16513.
10 C. G. Hu, L. X. Wang, Y. Zhao, M. H. Ye, Q. Chen, Z. H. Feng and L. T. Qu, *Nanoscale*, 2014, **6**, 8002.
11 W. Ma, Z. B. Gong, K. X. Gao, L. Qiang, J. Y. Zhang and S. R. Yu, *Mater. Lett.*, 2017, **195**, 220.
12 Z. A. Qiao, B. K. Guo, A. J. Binder, J. H. Chen, G. M. Veith and S. Dai, *Nano Lett.*, 2013, **13**(1), 207.
13 E. Bailón-García, A. Elmouwahidi, F. Carrasco-Marín, A. F. Pérez-Cadenas and F. J. Maldonado-Hódar, *Appl. Catal., B*, 2017, **217**, 540.
14 C. S. Lei, X. F. Zhu, B. C. Zhu, J. G. Yu and W. K. Ho, *J. Colloid Interface Sci.*, 2015, **466**, 238.
15 Z. H. Xu, J. G Yu, G. Liu, B. Cheng, P. Zhou and X. Y. Li, *Dalton Trans.*, 2013, **42**, 10190.
16 B. J. Dou, J. J. Li, Y. F. Wang, H. L. Wang, C. Y. Ma and Z. P. Hao, *J. Hazard. Mater.*, 2011, **196**, 194.
17 A. M. Ebrahim, B. Levasseur and T. J. Bandosz, *Langmuir*, 2013, **29**(23), 6895.
18 J. L. Lv, S. R. Zhai, Z. Z. Wang, Z. M. Lie and Q. D. An, *Res. Chem. Intermed.*, 2016, **42**(2), 839.
19 S. Yang, L. Wang, S. Yue, X. Guo, Y. Song and J. He, *RSC Adv.*, 2013, **3**, 16990.
20 S. X Yang, L. Y. Wang, X. D. Zhang, W. J. Yang and G. L. Song, *Chem. Eng. J.*, 2015, **275**, 315.
21 K. S. W. Sing, *Pure Appl. Chem.*, 1982, **54**(11), 2201.
22 L. H. Nie, A. Y. Meng, F. Teng and B. Cheng, *RSC Adv.*, 2015, **5**, 83997.
23 L. H. Nie, A. Y. Meng, J. G. Yu and M. Jaroniec, *Sci. Rep.*, 2013, **3**, 3215.
24 C. S. Lei, X. F. Zhu, B. C. Zhu, C. J. Jiang, Y. Le and J. G. Yu, *J. Hazard. Mater.*, 2017, **321**, 801.
25 L. H. Nie, Q. Tan, W. Zhu, Q. Wei and Z. K. Lin, *Acta Phys.-Chim. Sin.*, 2015, **31**(9), 1815.
26 S. Rani, K. Sumanjit and R. K. Mahajan, *Desalin. Water Treat.*, 2016, **57**(7), 3720.
27 L. H. Ai, Y. Zeng and J. Jiang, *Chem. Eng. J.*, 2014, **235**, 331.
28 Y. X. Zhang, S. X. Xu, Y. Y. Luo, S. S. Pan, H. L. Ding and G. H. Li, *J. Mater. Chem.*, 2011, **21**, 3664.
29 J. C. Hu, Z. Song, L. F. Chen, H. J. Yang, J. L. Li and R. Richards, *J. Chem. Eng. Data*, 2010, **55**(9), 3742.
30 C. S. Lei, M. Pi, C. J. Jiang, B. Cheng and J. G. Yu, *J. Colloid Interface Sci.*, 2017, **490**, 242.
31 H. M. Hu, G. Y. Chen, C. H. Deng, Y. Qian, M. Wang and Q. Zheng, *Mater. Lett.*, 2016, **170**, 139.
32 J. B. Fei, Y. Cui, J. Zhao, L. Gao, Y. Yang and J. B. Li, *J. Mater. Chem.*, 2011, **21**, 11742.
33 E. Lorenc-Grabowska and G. Gryglewicz, *Dyes Pigm.*, 2007, **74**(1), 34.
34 Q. J. Du, J. K. Sun, Y. H. Li, X. X. Yang, X. H. Wang, Z. H. Wang and L. H. Xia, *Chem. Eng. J.*, 2014, **245**, 99.
35 S. H. Kim and P. P. Choi, *Dalton Trans.*, 2017, **46**, 15470.
36 N. Dehghanian, M. Ghaedi, A. Ansari, A. Ghaedi, A. Vafaei, M. Asif, S. Agarwal, I. Tyagi and V. K. Gupta, *Desalin. Water Treat.*, 2016, **57**(20), 9272.
37 B. Ding, C. Guo, S. X. Liu, Y. Cheng, X. X. Wu, X. M. Su, Y. Y. Liu and Y. Li, *RSC Adv.*, 2016, **6**(40), 33888.
38 C. S. Lei, X. F. Zhu, Y. Le, B. C. Zhu, J. G. Yu and W. K. Ho, *RSC Adv.*, 2016, **6**(13), 10272.
39 Q. F. Peng, F. Yu, B. C. Huang and J. G. Yu, *RSC Adv.*, 2017, **7**(43), 26968.
40 C. S. Lei, M. Pi, B. Cheng, C. J. Jiang and J. Q. Qin, *Appl. Surf. Sci.*, 2018, **435**, 1002.
41 J. Xu, D. F. Xu, B. C. Zhu, B. C. Cheng and C. J. Jiang, *Appl. Surf. Sci.*, 2018, **435**, 1136.
42 C. S. Lei, M. Pi, D. F. Xu, C. J. Jiang and B. Cheng, *Appl. Surf. Sci.*, 2017, **426**, 360.
43 H. Chen, Y. Q. Zheng, B. Cheng, J. G. Yu and C. J. Jiang, *J. Alloys Compd.*, 2018, **735**, 1041.
44 Y. Q. Zheng, B. C. Zhu, H. Chen, W. You, C. J. Jiang and J. G. Yu, *J. Colloid Interface Sci.*, 2017, **504**, 688.
45 M. D. Liu, J. Xu, B. Cheng, W. K. Ho and J. G. Yu, *Appl. Surf. Sci.*, 2015, **332**, 121.